



Single-Shot Through-Focus Image Acquisition and Phase Retrieval From Chromatic Aberration and Multi-Angle Illumination

Guocheng Zhou¹, Shaohui Zhang^{1*}, Yayu Zhai², Yao Hu¹ and Qun Hao¹

¹ School of Optics and Photonics, Beijing Institute of Technology, Beijing, China, ² Research Center of Ship Quality and Reliability, China Institute of Marine Technology and Economy, Beijing, China

OPEN ACCESS

Edited by:

Chao Zuo,
Nanjing University of Science and
Technology, China

Reviewed by:

Yao Fan,
Nanjing University of Science and
Technology, China
Jinli Suo,
Tsinghua University, China

*Correspondence:

Shaohui Zhang
zhangshaohui@bit.edu.cn

Specialty section:

This article was submitted to
Optics and Photonics,
a section of the journal
Frontiers in Physics

Received: 02 January 2021

Accepted: 03 March 2021

Published: 29 April 2021

Citation:

Zhou G, Zhang S, Zhai Y, Hu Y and
Hao Q (2021) Single-Shot
Through-Focus Image Acquisition and
Phase Retrieval From Chromatic
Aberration and Multi-Angle
Illumination. *Front. Phys.* 9:648827.
doi: 10.3389/fphy.2021.648827

Phase recovery from a stack of through-focus intensity images is an effective non-interference quantitative phase imaging strategy. Nevertheless, the implementations of these methods are expensive and time-consuming because the distance between each through-focus plane has to be guaranteed by precision mechanical moving devices, and the multiple images must be acquired sequentially. In this article, we propose a single-shot through-focus intensity image stack acquisition strategy without any precision movement. Isolated LED units are used to illuminate the sample in different colors from different angles. Due to the chromatic aberration characteristics of the objective, the color-channel defocus images on the theoretical imaging plane are mutually laterally shifted. By calculating the shift amount of each sub-image area in each color channel, the distances between each through-focus image can be obtained, which is a critical parameter in transport of intensity equation (TIE) and alternating projection (AP). Lastly, AP is used to recover the phase distribution and realize the 3D localization of different defocus distances of the sample under test as an example. Both simulation and experiments are conducted to verify the feasibility of the proposed method.

Keywords: phase retrieval, alternating projection, chromatic aberration, single-shot, computational imaging, microscopy

INTRODUCTION

Quantitative phase imaging (QPI) [1] is crucial to label-free microscopic imaging in biomedical fields. In general, for light field passing through a transparent sample, the phase modulation caused by the sample refractive index distribution carries more effective information than the intensity modulation caused by the sample absorption distribution. Nevertheless, instead of phase distributions, we can only obtain intensity distributions with any existing photodetectors due to the extremely fast oscillations of light. Since the early 1900s, a lot of phase imaging methods converting phase to intensity measurement have been proposed [2–7]. It can be roughly classified into two categories. One is contrast phase measurement methods, such as phase-contrast microscopy [8]. Another one is quantitative phase measurement, including interferometry [9], Shack–Hartmann wave front sensor (SHWFS) [10, 11], and so on. The measurement accuracy of interferometry is high, but it is sensitive to environmental noises and suffers from an unwrapping problem. Compared with interferometry, SHWFS and phase-contrast microscopy have relatively simple

system constructions and superior anti-jamming characteristics, but the measurement accuracy of SHWFS is relatively low and phase-contrast microscopy can only achieve a qualitative phase. Therefore, phase imaging with the characteristics of simple structure and strong robustness to noise and environmental disturbances has always been pursued by researchers.

Compared with the conventional methods mentioned above, phase retrieval methods rooting in diffraction have been used widely due to their high anti-jamming capability and good performance, including Fourier ptychographic imaging (FPM) [12–14], ptychographic iterative engine (PIE) [15–18], and so on. PIE aims to retrieve the phase distribution from a series of diffraction patterns corresponding to illumination situations with different positions but a certain overlap ratio between adjacent illumination probes. FPM, sharing its root with phase retrieval and synthetic aperture imaging, can realize a high-resolution (HR), large field-of-view (FOV) amplitude and phase of an object simultaneously. Although PIE and FPM are widely used in quantitative phase imaging, a key problem involved is the time-consuming data acquisition process. In comparison, some phase retrieval methods based on through-focus diversity have also been proposed. Transport of intensity equation (TIE) [19–23] can realize robust phase recovery by constructing the relationship between phase distribution and the differential of light distribution along the optical axis. The axial intensity differential can be equivalent realized by the difference between two through-focus intensity images. Different from the above strategy that calculates phase distribution directly from clear physical models, another kind of phase imaging strategy is realized through the optimization strategy of round-trip iterative constraints between two or more through-focus intensity images. Typical optimization algorithms include the Gerchberg–Saxton (GS) rooting in alternating projection (AP) or projection onto convex sets (POCS), averaged projection, averaged reflection and relaxed averaged alternating reflection (RAAR), etc. [24]. Nevertheless, both TIE and iteration optimization methods need to mechanically scan a camera or sample to obtain the through-focus intensity images, which relies on a precision mechanical moving device.

In order to avoid mechanical scanning and reduce data acquisition time, several methods based on single-shot through-focus intensity image acquisition have been proposed. For example, Waller et al. used chromatic aberration of objective to acquire three raw images simultaneously [25]. Komuro et al. realized TIE phase retrieval with multiple bandpass filters [26] and polarization-directed flat lenses [27, 28]. However, the above methods still require precise mechanical movement calibration of the defocus distance of the system in advance, which is complicated and time-consuming. What is more, the relative distances between each color channel are also related to the overall defocus distance of the sample, which cannot be obtained in a single measurement.

In this paper, we propose a single-shot phase retrieval method based on chromatic aberration and image lateral shift resulting from the multi-angle illuminations of the out-of-focus sample. A sample located at a defocus position is illuminated by light sources of different wavelengths from different incident angles

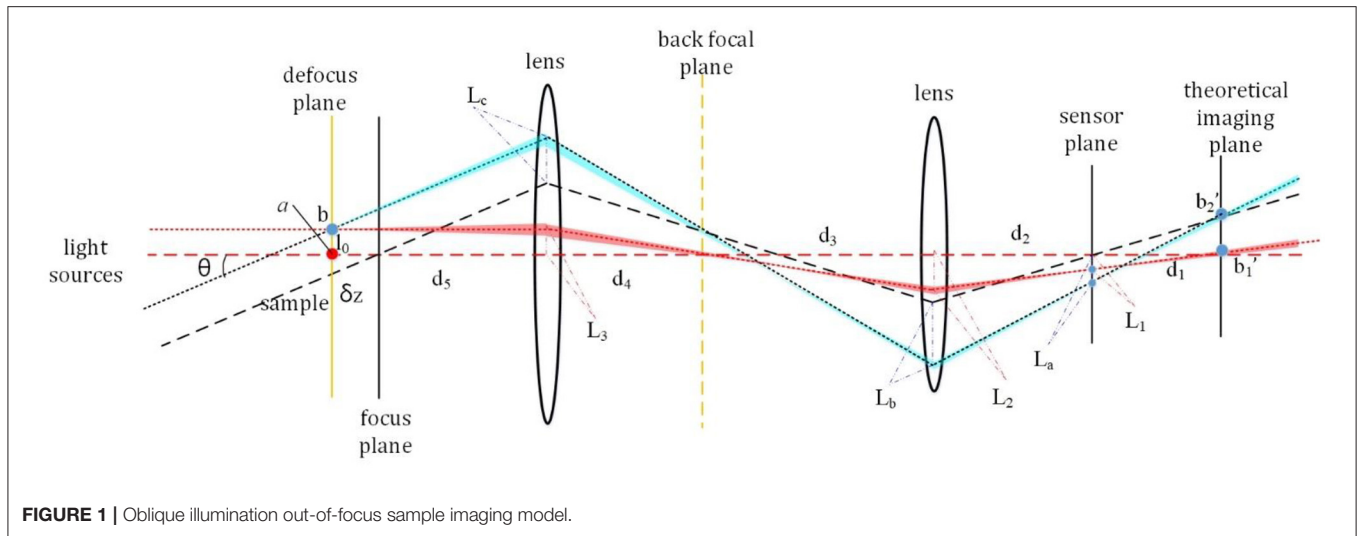
and then imaged with an RGB (red, green, blue) color camera through a microscopic objective. Due to the chromatic aberration of the objective and the different illumination angles, three monochromatic intensity images (red, green, and blue) can be extracted from a single-frame color image. By calculating the lateral shift of each section of the sample, the relative defocus distance between the focus plane and the channel planes can be obtained mathematically. Benefiting from this strategy, defocus distances can be obtained easily without any mechanical moving device and precise measurement. Then, the AP phase retrieval algorithm is utilized to realize phase distribution recovery. Lastly, three-dimensional (3D) localization of the sample can also be obtained. Furthermore, we also improve the Fresnel transfer function (TF) propagator in the AP phase retrieval algorithm in order to accommodate the angle-varied illuminations and out-of-focus samples. This paper is organized as follows: the optical imaging model with angle-varied illuminations is presented in section Oblique Illumination Model. The SAD image registration method used for calculating the image lateral shift is presented in section SAD Image Registration. Color cross-talk in the RGB camera and the AP phase retrieval framework with improved Fresnel TF propagator are presented in sections Color Cross-Talk Elimination and Alternating Projection Phase Retrieval Algorithm, respectively. Section Simulation Experiment presents the simulations to demonstrate the feasibility of the proposed method. We use biological samples in section Experiments to prove the success of phase retrieval experimentally. Finally, the conclusion and discussion are summarized in section Conclusion and Discussion.

PRINCIPLE

Oblique Illumination Model

As shown in **Figure 1**, we build a model to illustrate how the defocus distance and illumination angles affect the image lateral shift in microscopy. If a sample is placed at an out-of-focus position, the images corresponding to illuminations from different angles will have a relative lateral shift between each other. Zheng et al. also realized auto-focusing for microscopic imaging with the lateral shift amount as a defocus distance criterion [29].

A sample is placed at a defocus plane and illuminated by two light beams with the same wavelength, but different incident angles simultaneously, as shown in **Figure 1**. δz is the defocus distance and θ is the angle between two incident light sources. d_1 is the distance between the sensor plane and the theoretical imaging plane. d_2 , d_3 , d_4 , and d_5 are system parameters corresponding to the microscopic system. Assuming there are two points of the sample, a and b . a locates at the optical axis, and the distance between a and b is l_0 . b_1' and b_2' are two imaging points corresponding to point b with different incident angles at the theoretical imaging plane. If the sample is placed at the focus plane, both axial points and off-axis points have no lateral shift at the theoretical imaging plane. Thus, b_1' and b_2' will coincide at the theoretical imaging plane. But if the sample is placed at an out-of-focus plane, a lateral shift between b_1' and b_2' will appear. As shown in **Figure 1**, the lateral shift



between b_1' and b_2' at the sensor plane is defined as $\delta L = L_a - L_1$. We can derive some equations connecting the above-mentioned variables together.

$$\begin{cases} \frac{L_1}{L_2} = \frac{d_1}{d_1+d_2} \\ \frac{L_2}{L_3} = \frac{d_3}{d_4} \\ L_3 = l_0 \end{cases}, \quad \begin{cases} \frac{L_a}{L_b} = \frac{d_1}{d_1+d_2} \\ \frac{L_b}{L_c} = \frac{d_3}{d_4} \\ L_c = l_0 + \delta z \cdot \tan\theta \end{cases} \quad (1)$$

Equation (1) can be further organized as follows:

$$\delta L = L_a - L_1 = \frac{d_1 \cdot d_3}{d_4 \cdot (d_1 + d_2)} \cdot \tan\theta \cdot \delta z = \xi \cdot \tan\theta \cdot \delta z \quad (2)$$

where $\xi = \frac{d_1 \cdot d_3}{d_4 \cdot (d_1 + d_2)}$ is a constant value corresponding to each specific wavelength. It will have different values for different wavelengths due to the chromatic aberration characteristics of the objective. Essentially, Equation (2) aims to calculate the defocus distance δz from d_1 . Due to the microscopy and the camera forming an integrated system, the axial defocus distance d_1 is difficult to measure directly. Therefore, we transform calculating d_1 to the lateral distance δL in Equation (2). Given that the AP algorithm framework requires at least two through-focus intensity images to be implemented, we utilize three-wavelength light-emitting diodes (LEDs) corresponding to the three channels of the RGB camera to illuminate the out-of-focus sample from different directions respectively. As shown in **Figure 2**, a red LED is placed at the optical axis, and the corresponding defocus image is used as a reference value because of the characteristic that the defocus image illuminated by normal incidence illumination will not have a lateral shift relative to the focused image. One green LED and one blue LED are placed at the two off-axis positions to provide oblique illuminations, in which the incident illumination angles are θ_{rg} and θ_{rb} , respectively. The defocus distances δz_{fg} and δz_{fb} between the focus plane and the green/blue channel images can be calculated through Equation (3). We should emphasize that benefiting from the normal incidence illumination corresponding to red LED, although the red channel

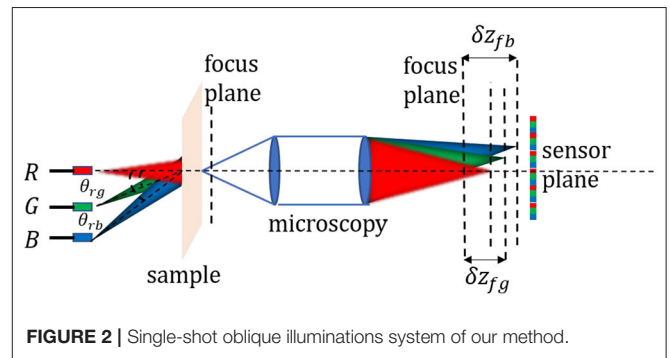
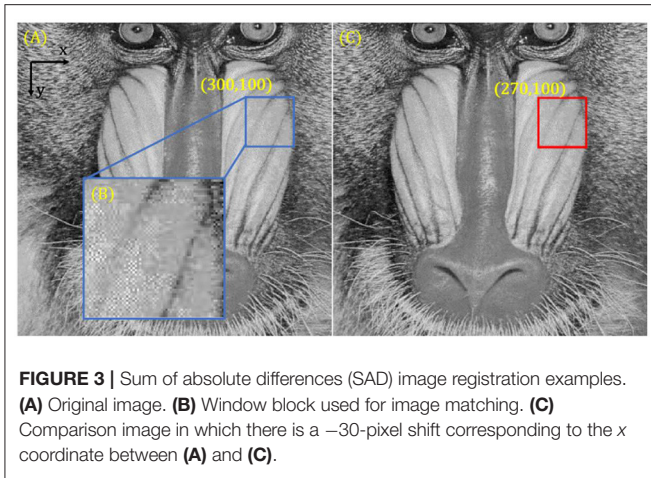


image is located at the out-of-focus position, there exists no lateral shift compared with the focus image. The red channel image can be used as a reference value to calculate the defocus distances between the focus plane and the green/blue channel images. Therefore, we transform calculating the lateral shift between the focus image and the green/blue channel image to calculating the lateral shift between the red and green/blue channel images. Equation (3) indicates that the lateral shifts of the green and blue channels relative to the red image are proportional to the defocus distances between the focus plane and the green/blue channel image, where A_{ri} is a constant value decided by the incident angle and wavelength.

$$\delta L_{ri} = \xi_{ri} \cdot \tan\theta_{ri} \cdot \delta z_{fi} = A_{ri} \cdot \delta z_{fi}, \quad (i = g, b) \quad (3)$$

SAD Image Registration

According to the above-mentioned illumination direction and the wavelength multiplexing strategy in section Oblique Illumination Model, we can obtain the defocus distances by calculating the lateral shifts between the red and green/blue channel images. To obtain the precise shifts between different images, we use the sum of absolute differences (SAD) to realize image matching [30, 31]. SAD is a widely used, extremely



simple video quality metric used for block matching in motion estimation for video compression. It works by taking the absolute value of the difference between each pixel in the original block and the corresponding pixel in the block being used for matching. As shown in Equation (4), $S(i + s - 1, j + t - 1)$ is one pixel value of the original block and $T(s, t)$ is the corresponding pixel in the block for comparison.

$$D(i, j) = \sum_{s=1}^M \sum_{t=1}^N |S(i + s - 1, j + t - 1) - T(s, t)|, \quad (1 \leq i \leq m - M + 1, 1 \leq j \leq n - N + 1) \quad (4)$$

We show a simulation example of the SAD image registration strategy in **Figure 3**. **Figures 3A,C** are the original and comparison images, respectively. A window block in **Figure 3A** is enlarged, as shown in **Figure 3B**, whose coordinates of the top left corner is (300, 100). Then, we search for window blocks in different positions in **Figure 3C** and calculate the SAD value between them and **Figure 3B**. Finally, we can find the optimal block, whose coordinates of the top left corner is (270, 100). The red boxed sub-region in **Figure 3C**, owning the minimum SAD value with **Figure 3B**, is the best-matched block corresponding to **Figure 3B**. The relative pixel position shift between the matching block pair is (-30, 0), which is consistent with the set value. Assigning a value to pixel size, we can calculate the defocus distance according to Equation (3). Given the discrete sampling process of a digital camera sensor, Equation (3) can be rewritten as follows:

$$\delta L_{ri} = P_{s_{ri}} \cdot S_p = A_{ri} \cdot \delta z_{fi}, \quad (i = g, b) \quad (5)$$

where $P_{s_{ri}}$ is the pixel shift between the red channel and the green/blue channels and S_p is the pixel size of the RGB camera we used in the following experimental section.

Color Cross-Talk Elimination

Generally speaking, the most common color industrial camera is combined with a Bayer filter and a complementary metal

TABLE 1 | Color cross-talk matrix W of our RGB camera.

	626, 517, 470 nm		
W	1.0000	0.1462	0.0242
	0.0987	1.0000	0.3292
	0.0414	0.2931	1.0000

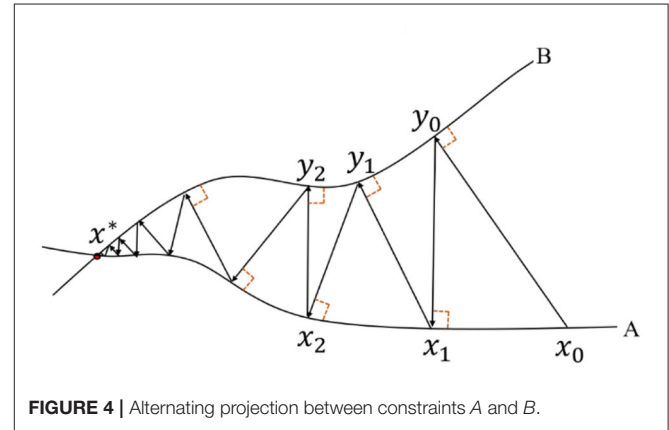


FIGURE 4 | Alternating projection between constraints A and B.

oxide semiconductor (CMOS) sensor. However, due to the color separation performance of the Bayer filter being imperfect, color cross-talk or color leakage will exist among each of the color channels (i.e., red, green, and blue) [32, 33]. Thus, eliminating the color cross-talk among the RGB channels before separating them is important in our proposed method. The imaging process of RGB oblique illumination with a color camera can be mathematically described as follows:

$$\begin{bmatrix} M_R \\ M_G \\ M_B \end{bmatrix} = \mathbf{W} \cdot \begin{bmatrix} I_r \\ I_g \\ I_b \end{bmatrix} = \begin{bmatrix} R_r & R_g & R_b \\ G_r & G_g & G_b \\ B_r & B_g & B_b \end{bmatrix} \cdot \begin{bmatrix} I_r \\ I_g \\ I_b \end{bmatrix} \quad (6)$$

where \mathbf{W} is the color cross-talk matrix between the RGB channels. M_R , M_G , and M_B are the RGB channels captured by the color camera, and the subscripts R, G, and B indicate the red, green, and blue channels, respectively. I_r , I_g , and I_b are the illumination intensities in front of the Bayer filter corresponding to red, green, and blue colors, respectively. The illumination parameters in the color cross-talk matrix \mathbf{W} can be obtained experimentally by a spectrometer or calculated using Equation (7), where the superscript “-1” refers to the inverse matrix.

$$\mathbf{W} = \begin{bmatrix} R_r & R_g & R_b \\ G_r & G_g & G_b \\ B_r & B_g & B_b \end{bmatrix} = \begin{bmatrix} M_R \\ M_G \\ M_B \end{bmatrix} \cdot \begin{bmatrix} I_r \\ I_g \\ I_b \end{bmatrix}^{-1} \quad (7)$$

In our experiment, a color camera (FLIR, BFS-U3-200S6C-C) is used for recording images. The matrix \mathbf{W} corresponding to the wavelengths of the RGB LED (470, 517, and 626 nm, respectively) is shown in **Table 1**.

Alternating Projection Phase Retrieval Algorithm

Alternating projection is a kind of optimization strategy realized by sequentially projecting onto several constraints back and forth multiple times. It has been utilized in performing phase retrieval by means of through-focus intensity images [34, 35]. The simplest case of AP involves two constraints, curves *A* and *B*, as shown in **Figure 4**. The intersection point x^* of two constraints indicates the optimal solution of this case. The AP framework can start with an initial guess, x_0 , and then projecting x_0 between constraints *A* and *B* sequentially. The optimal solution x^* can be found finally as shown in **Figure 4**. Actually, in real experiments, three or more physical constraints can be utilized in the AP

process to help improve the possibility of jumping out of the local optimal solution and increase the convergence efficiency, which is also named “sequential projection” or “cyclic projection.”

The information of a sample under test can be represented by a 3D transmittance distribution, which can be written as Equation (8).

$$U(\vec{r}) = A_m \cdot e^{j \cdot \vec{k} \cdot \vec{r}} \quad (8)$$

where A_m is the amplitude transmittance of the object and $e^{j \cdot \vec{k} \cdot \vec{r}}$ refers to the phase transmittance part. $k = \frac{2\pi}{\lambda}$ is the wave vector, where λ indicates the illumination wavelength. Vector \vec{r} denotes the 3D position. Combining with the Fresnel TF propagator, we can propagate the complex light field to different positions and obtain several field distributions corresponding to the different defocus distances [36]. A common propagation routine can be expressed as Equation (9).

$$U_2(x, y) = I^{-1} \{ I \{ U_1(x, y) \} H(f_x, f_y) \} \quad (9)$$

where (x, y) indicates a 2D plane, $U_1(x, y)$ is the original field distribution, and $U_2(x, y)$ is the field in a distance observation plane. The transfer function H is described as Equation (10), where z is the propagation distance from the $U_1(x, y)$ plane to the $U_2(x, y)$ plane.

$$H(f_x, f_y) = e^{jkz} \exp \left[-j\pi\lambda z (f_x^2 + f_y^2) \right]. \quad (10)$$

The propagator H shown in Equation (10) is applied to a wide range of propagation scenarios that accommodate normal

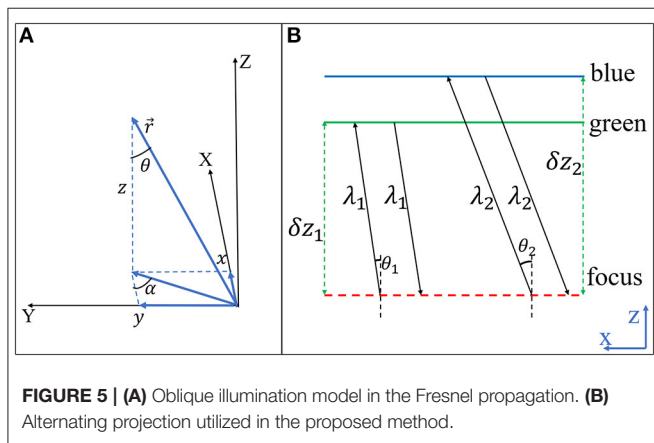


FIGURE 5 | (A) Oblique illumination model in the Fresnel propagation. **(B)** Alternating projection utilized in the proposed method.

Algorithm outline

Input: Through-focus image data I_1, I_2 ; defocus distance $\delta z_1, \delta z_2$;

illumination angles $\alpha_1, \alpha_2, \theta_1, \theta_2$; illumination wavelengths λ_1, λ_2 ;

Output: Updated object $U_{updated}(x, y)$, including amplitude and phase respectively;

The Fresnel propagator: $H_n(\delta z_n, \alpha_n, \theta_n, \lambda_n) = e^{jk_z \delta z_n} e^{j\delta z_n(k_x \cos \alpha_n + k_y \sin \alpha_n) \tan \theta_n}$, ($n = 1, 2$);

Initialize $U_{updated}(x, y) = A e^{j\varphi}$ at focus plane, where A and φ are two all ones matrix.

for $i = 1$: loopNum

for $j = 1$: 2

project object onto plane j : $U_j(x, y) = \mathfrak{F}^{-1} \{ \mathfrak{F} \{ U_{updated}(x, y) \} H_j(\delta z_j, \alpha_j, \theta_j, \lambda_j) \} = A_j e^{j\varphi_j}$;

replace amplitude and keep phase unchanged: $U_{j_new}(x, y) = \sqrt{I_j} \cdot e^{j\varphi_j}$;

project $U_{j_new}(x, y)$ onto focus plane: $U_{updated}(x, y) = \mathfrak{F}^{-1} \{ \mathfrak{F} \{ U_{j_new}(x, y) \} H_j(-\delta z_j, \alpha_j, \theta_j, \lambda_j) \}$;

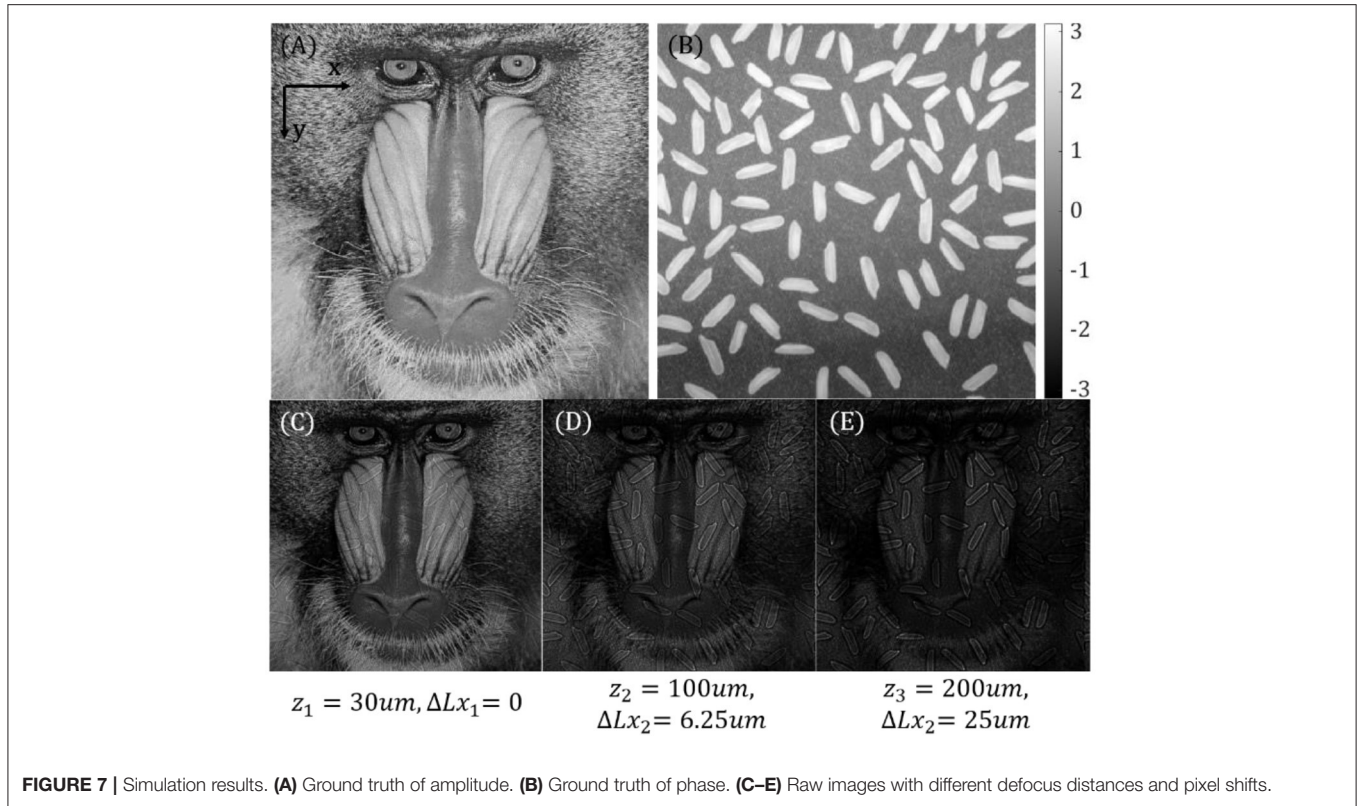
end

end

Amplitude_recovered = abs($U_{updated}(x, y)$);

Phase_recovered = angle($U_{updated}(x, y)$);

FIGURE 6 | Algorithm outlines of alternating projection in phase retrieval.



incidence illuminations. However, in angle-varied illuminations, if a sample is placed at the defocus plane, oblique illumination will result in not only a lateral shift in the spatial domain but also a spectrum shift in the Fourier domain. Thus, to solve the spectrum shift, the propagator should be improved.

According to the Fresnel TF propagator with angle-varied illuminations, the phase function can be described as shown in Equation (11), where k_x, k_y are components of the wave vector corresponding to the x -axis and y -axis, respectively.

$$\Phi(x, y) = k_x x + k_y y \quad (11)$$

As shown in **Figure 5A**, $|\vec{r}|$ is the radial distance in the observation plane from the origin to the beam aiming point and z is the perpendicular distance between two planes. Equation (11) can be rewritten as follows, where $\alpha = \tan^{-1}(\frac{y}{x})$ and θ indicates the illumination angle.

$$\Phi(k_x, k_y) = z(k_x \cos \alpha + k_y \sin \alpha) \tan \theta \quad (12)$$

The propagator in our strategy should be improved as Equation (13), where $k_z^2 = k^2 - k_x^2 - k_y^2$.

$$H(k_x, k_y) = e^{jk_z z} \cdot e^{jz(k_x \cos \alpha + k_y \sin \alpha) \tan \theta} \quad (13)$$

To obtain several constraints in the optical imaging process, we can propagate the complex light field to different positions by the propagator in Equation (13) and record the corresponding intensity image stack. For instance, as shown in **Figure 5B**, we set

$\alpha = 0$. By utilizing the axial chromatic aberration characteristics, we use two channels (green and blue) of the same planar sensor to record the intensity images corresponding to the different propagation distances with different illumination angles. The perpendicular defocus distance δz_n between the focus plane and the green/blue channels can be calculated by Equation (3). Intensity images obtained with a digital image sensor can directly be expressed as Equation (14).

$$I_n = |I^{-1} \{I \{U(x, y)\} H_n(k_x, k_y)\}|^2, \quad n = 1, 2, \quad (14)$$

where the intensity images I_1, I_2 that correspond to the green and blue channels form two constraints, respectively. $H_n(k_x, k_y)$ is the Fresnel propagator with different illumination angles and distances. Thus, according to **Figure 5B**, the framework of the alternating projection phase retrieval approach can be expressed as the process shown in **Figure 6**, where *Amplitude_recovered* and *Phase_recovered* are the recovered amplitude and phase of the sample. *loopNum* is an iteration number (typical values are 10, 20, and so on).

SIMULATION EXPERIMENT

Consistent with the systematic parameters in the experiments, the illumination wavelengths are set to 470, 517, and 626 nm in simulation. The pixel size of the RGB camera is 2.4 μm . The distance between the illumination source and the sample plane is 80 mm. According to **Figure 2**, a red LED unit is placed on the

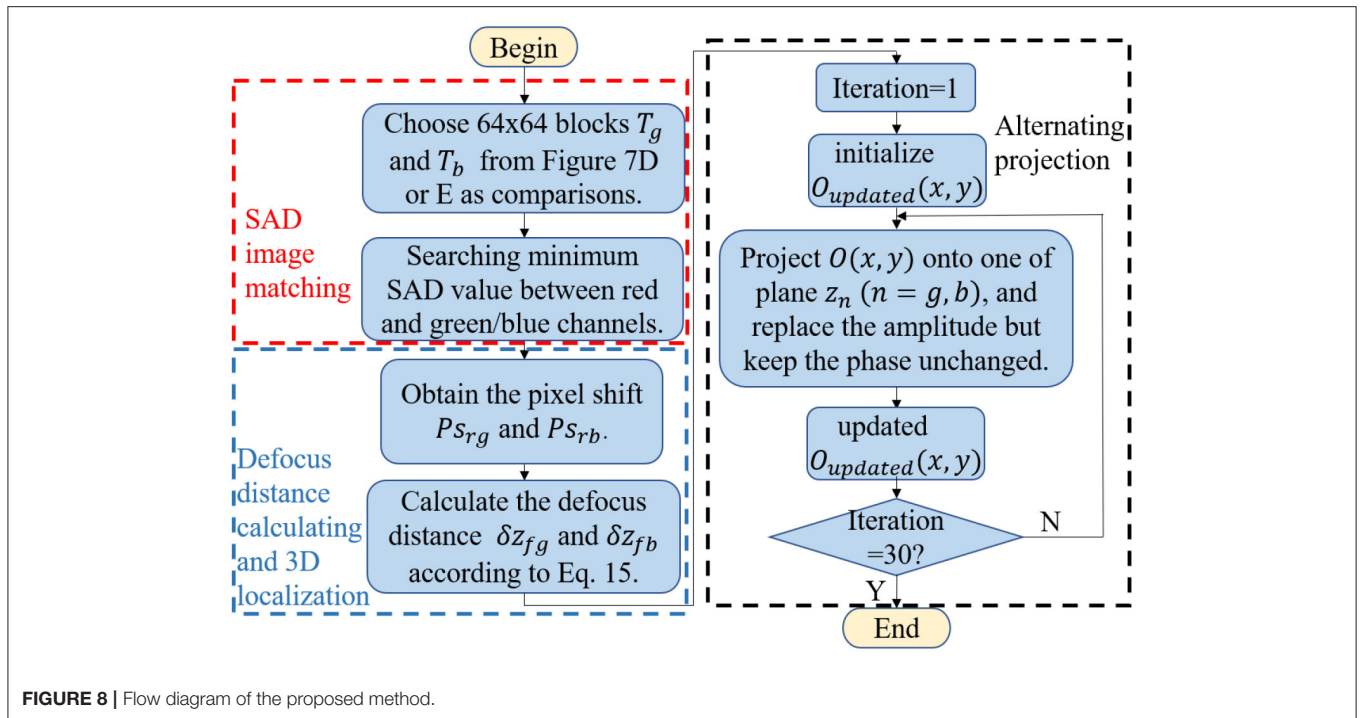


FIGURE 8 | Flow diagram of the proposed method.

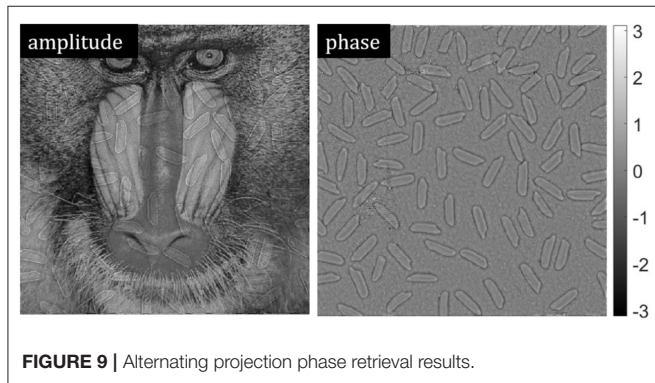


FIGURE 9 | Alternating projection phase retrieval results.

optical axis, in which the corresponding channel image is used as a reference. The x -dimension lateral distance between the red and green LED is set to $Dx_{rg} = 5 \text{ mm}$ and the y -dimension distance is set to $Dy_{rg} = 0 \text{ mm}$, which means α is set to 0. In a similar way, we set $Dx_{rb} = 10 \text{ mm}$ and $Dy_{rb} = 0 \text{ mm}$, where $r, g,$ and b indicate the red, green, and blue light source, respectively. Therefore, the tangent functions of the illumination direction angles in Figure 2 are $\tan \theta_{rg} = \frac{5}{80}$ and $\tan \theta_{rb} = \frac{10}{80}$, respectively. In the simulations, we assume that the scale factor $\xi = 1$. Thus, Equation (3) can be rewritten as follows:

$$\delta L_{ri} = Ps_{ri} \cdot S_p = \tan \theta_{ri} \cdot \delta z_{fi}, \quad (i = g, b) \quad (15)$$

As shown in Figures 7A,B, the “baboon” and “rice” images are used as the ground truth of the amplitude and phase parts, respectively. Their image size is set to 512×512 . By using

the Fresnel diffraction equation shown in Equation (14), we obtain three intensity images at different axial positions, as shown in Figures 7C–E. As mentioned above, Figure 7C belongs to the red channel image, which is illuminated by the normal incidence illumination. Thus, Figure 7C is used as the reference to calculate the defocus distances between the focus plane and the green/blue image planes. The equivalent defocus distances between the focus plane and each image plane is set as $z_i = [30, 100, 200] \text{ um}$, $(i = r, g, b)$. And the x -dimension separation between the focus plane and each channel image can be written as $Lx_i = [0, 6.25, 25] \text{ um}$, $(i = r, g, b)$, according to Equation (15), while the y -dimension separations are 0. Thus, the relative pixel shifts between the red and green/blue channels can be calculated as $Ps_{ri} = [2.6, 10.4] \text{ pixels}$ $(i = g, b)$, theoretically. Considering the discrete sampling property of digital cameras, pixel shifts should be rounded as $Ps_{ri} = [3, 10] \text{ pixels}$ $(i = g, b)$. In general, Figures 7C–E are the final raw data corresponding to the red, green, and blue channels, respectively, which involve different defocus distances and pixel shifts in our simulations.

Figure 8 shows the flow diagram of the proposed method. We chose two 64×64 window blocks T_g and T_b as comparisons from Figures 7D,E, respectively, which is similar to that in section SAD Image Registration. Then, according to Equation (4), by searching for the optimal window blocks that have the minimum SAD values with T_g and T_b in the red channel intensity image, we can obtain the pixel shifts Ps_{rg}, Ps_{rb} between the red channel and the green/blue channels. The absolute defocus distance between the focus plane and the green/blue channels, $\delta z_{fg}, \delta z_{fb}$, can be calculated by Equation (15). For example, in our simulations, the pixel shifts we calculated are $Ps_{rg} = 3 \text{ pixels}$ and $Ps_{rb} = 10 \text{ pixels}$, which conform to the parameters we simulated. And according

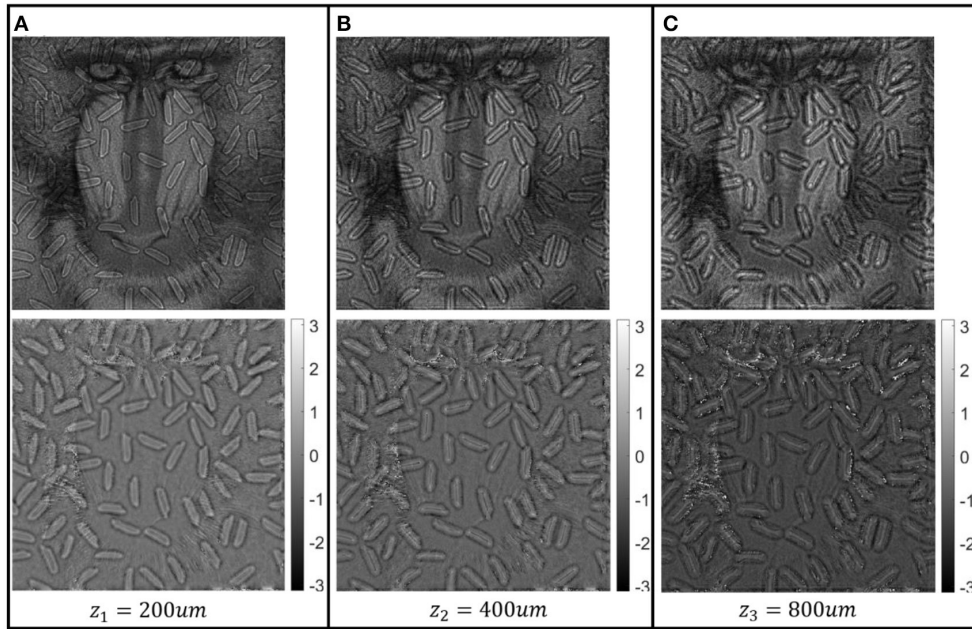


FIGURE 10 | (A–C) Amplitude and phase of the sample corresponding to defocus distances of 200, 400, and 800 μm , respectively.

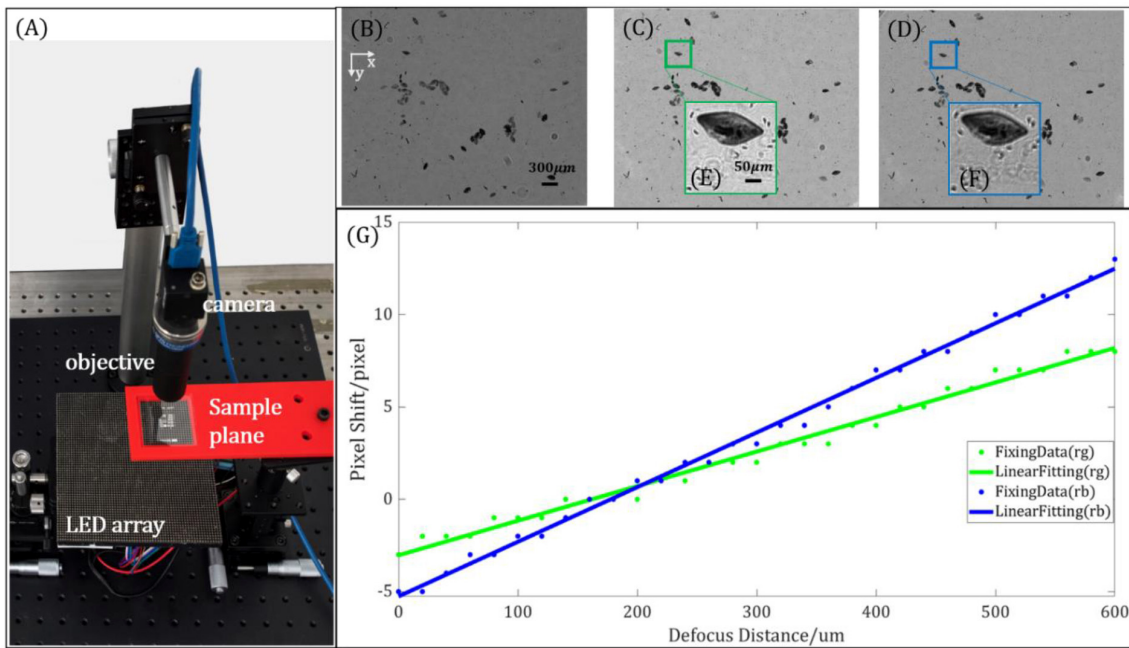


FIGURE 11 | Scale factor calibration results. **(A)** System setup of the proposed method. **(B–D)** Through-focus images corresponding to the red, green, and blue channels, respectively; **(B)** is the reference image for the sum of absolute differences (SAD) image matching. **(E)** Window block from the green channel used for SAD image matching. **(F)** Window block from the blue channel. **(G)** Linear fitting results corresponding to system parameters A_{rg} and A_{rb} .

to Equation (15), the absolute defocus distances we obtained are $\delta z_{fg} = 115 \mu\text{m}$ and $\delta z_{fb} = 192 \mu\text{m}$, which are approximately equal to the ideal values. This error comes from the round-off operation to non-integer pixel data.

In accordance with the defocus distance obtained above, AP phase retrieval approaches are used for phase recovery. According to section Alternating Projection Phase Retrieval Algorithm, two images corresponding to the green and blue

TABLE 2 | Relationship of the defocus distance and pixel shift.

$\delta z/\mu\text{m}$	0	20	40	60	80	100	120	140
Pixel shift	−5	−5	−4	−3	−3	−2	−2	−1
$\delta z/\mu\text{m}$	160	180	200	220	240	260	280	300
Pixel shift	−1	0	0	1	1	2	3	3
$\delta z/\mu\text{m}$	320	340	360	380	400	420	440	460
Pixel shift	4	4	5	5	6	7	8	8
$\delta z/\mu\text{m}$	480	500	520	540	560	580	600	
Pixel shift	9	9	10	11	11	12	13	

channels are used as amplitude constraints, which means that the amplitude of the complex light field to be recovered at the same axial position should be equal to the square root of the image intensity value. We give an initial guess of the sample's complex function firstly at the focus plane, and then projecting it onto the green (or blue) plane position, replacing the amplitude part with the measured value while keeping the phase part unchanged, and then projecting it back to the focus plane. By repeating this procedure, we can obtain an updated object complex function. Through multiple projections and amplitude replacements between the focal plane and the corresponding constraints of the blue and green channels, we can obtain a final solution. The amplitude and the phase part recovered with the above approach are shown in **Figure 9**. The cross-talk between amplitude and phase may come from the calculation deviation of the SAD and the following error of defocus distance.

Furthermore, by propagating the recovered object function to the different defocus distances, we can also realize 3D localization in the proposed method. As shown in **Figure 10**, we propagate the recovered object function to 200, 400, and 800 μm with the illumination angle, θ_{rg} , and obtain both the amplitude and phase of the sample corresponding to the different defocus distances, respectively. Compared with the amplitude parts of the sample in **Figures 10A–C**, by changing the different propagation distances but the same incidence illumination angle, we found that our method can be used in refocusing. With the increase of the propagation distance, the lateral shift is clearer in the results. Furthermore, compared with the phase parts of the sample in **Figures 10A–C**, we found that the phase parts also change with the increase of the propagation distance. Generally, the results shown in **Figure 10** demonstrate the feasibility of our method by simulations in 3D localization.

EXPERIMENTS

To demonstrate the feasibility of our method in actual experiments, we use Paramecium and bee wing as samples for parameter calibration, phase imaging, and 3D localization. In our experiment, the optical system consists of an RGB camera (FLIR, BFS-U3-200S6C-C) for recording images, a telecentric objective with certain chromatic aberrations (OPTO, TC23004; magnification $\times 2$, NA ≈ 0.1 , FOV = 4.25 mm \times 3.55 mm, working distance = 56 mm) for imaging, and an RGB LED array

(CMN, $P = 2.5, 470, 517, \text{ and } 626 \text{ nm}$) for providing wavelength and direction multiplexing illumination. The system setup is shown in **Figure 11A**. The distance between the sample plane and the illumination LED plane is adjusted to 90 mm. According to **Figure 2**, red, green, and blue LEDs are used for angle-varied illuminations. Similar to the parameter set in the simulations, the y -dimension lateral distance between the red and green LEDs is set to $Dy_{rg} = 2.5 \text{ mm}$ and the x -dimension distance is set to $Dx_{rg} = 0 \text{ mm}$, which means α is set to 90° . We set $Dy_{rb} = 5 \text{ mm}$ and $Dx_{rb} = 0 \text{ mm}$, where r, g, and b indicate the red, green, and blue light sources, respectively. The red illumination light is normally incident onto the sample, while the tangent functions of the illumination angles are $\tan \theta_{rg} = \frac{2.5}{90}$ and $\tan \theta_{rb} = \frac{5}{90}$ for the green and blue lights, respectively. Before implementing Equation (3) to calculate the defocus distance for each channel, we should obtain the scale factors A_{rg} and A_{rb} first. As shown in **Figures 11B–G**, we use a Paramecium biological sample to realize the scale factor calibration. **Figures 11B–D** show the three monochromatic intensity images extracted from the RGB channels of the same image sensor, respectively. **Figure 11B** is the reference image corresponding to the red channel. **Figures 11E,F** are two window blocks we choose to search for the minimum SAD value between the red and green/blue channels, respectively. We change the defocus distance from 0 to 600 μm , in which step the size is set to 20 μm and we record the corresponding through-focus images. By implementing the SAD image registration method, we can calculate the pixel shift between the red and green/blue channels. **Table 2** is a set of SAD image matching results of the reference image and the blue channel image. As shown in **Figure 11G**, by using the linear fitting method, we can obtain the scale factor of the two different wavelengths as follows: $A_{rg} = 0.045$ and $A_{rb} = 0.071$. Then, combining with the results of the scale factor, we can obtain the defocus distance between the focus plane and the green/blue channel planes mathematically. Furthermore, according to **Figure 11G**, we found that the absolute defocus distances at the 0-pixel shift between the green and blue channels are different, which is caused by the chromatic aberration of objectives.

As shown in **Figure 12**, we use the biological sample bee wing to demonstrate the feasibility of our method. **Figures 12A,B** are raw data extracted from the RGB camera corresponding to the green and blue channels, respectively. By utilizing Equation (3), the defocus distances between the focus and the green/blue channel images are 256.6 and 324.6 μm , respectively. Then, as shown in **Figures 12C,D**, we use the AP phase retrieval approach to reconstruct both the amplitude and phase of the biological sample at the focus plane.

Furthermore, similar to the simulations shown in **Figure 10**, we choose several defocus distances as examples to perform 3D localization. As shown in **Figure 13**, after obtaining the recovered object function, we propagate it onto different defocus distances (such as $-200, 200, \text{ and } 400 \mu\text{m}$) with the illumination angle θ_{rg} . Both the amplitude and phase of the sample corresponding to the different defocus distances can be obtained by this procedure. As shown in **Figures 13A–C**, the enlarged red boxed sub-regions belong to the same sub-region in the amplitude of the sample while owning different defocus distances. We found that with

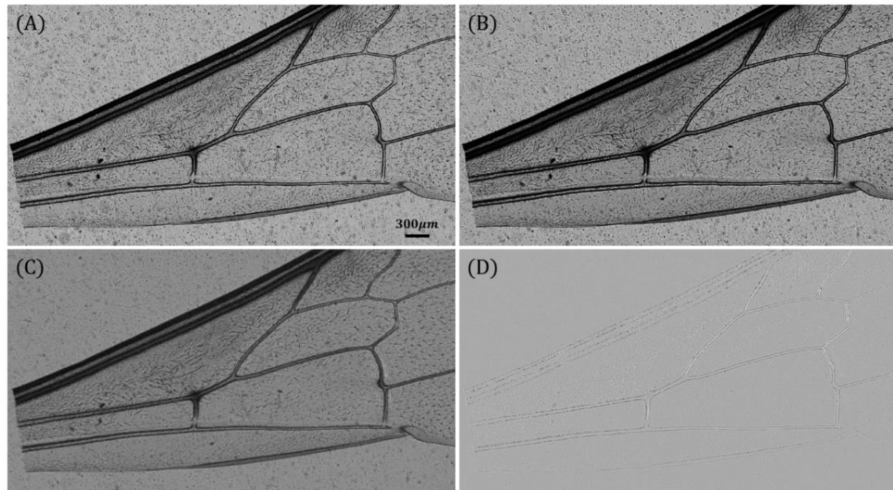


FIGURE 12 | (A,B) Images of the green and blue channels extracted from the RGB camera. (C) Amplitude of the recovered object. (D) Phase of the recovered object.

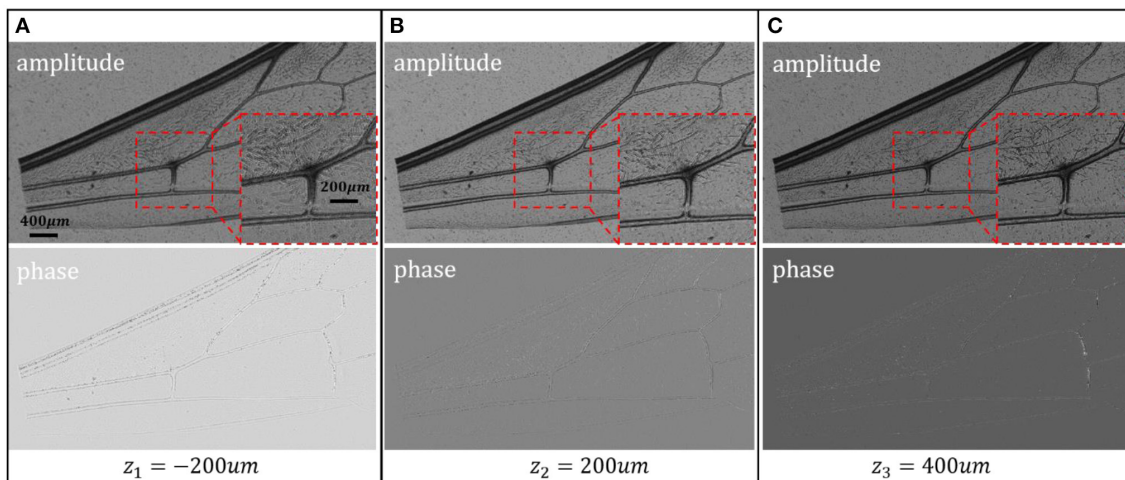


FIGURE 13 | Three-dimensional localization results of the biological sample. (A–C) Amplitude and phase of the sample corresponding to different defocus distances.

the change of defocus distance, both the amplitude and phase of the sample will be changed. Generally speaking, **Figure 13** demonstrates the feasibility of the proposed method in realizing a 3D localization in actual experiments.

CONCLUSION AND DISCUSSION

Generally speaking, through-focus intensity image acquisition methods play a critical role in AP and TIE phase retrieval approaches. In this paper, inspired by chromatic aberration of an objective and lateral shift resulting from the multi-angle illuminations of the out-of-focus sample, we proposed a single-shot through-focus intensity image acquisition strategy and realize phase recovery by the AP phase retrieval method. A Fresnel TF propagator corresponding to angle-varied illuminations is utilized in our method to solve the spectrum

shift in out-of-focus imaging with oblique illuminations. Three isolated LED units are used for illumination with different wavelengths from different incident angles. Due to the chromatic aberration of an objective, there will be a lateral shift between each color channel. The red channel image is used as a reference in the calculation of the lateral shift between the red and green/blue channel images because there is no lateral shift between the defocus image and the focus image if the sample is illuminated by a normal incidence illumination. Then, the defocus distances between the focus plane and the green/blue planes can be calculated by the lateral shift between the red and green/blue channel images mathematically. Compared with the proposed methods that utilize chromatic aberration while using three normal incidence illuminations, our method can obtain the defocus distances mathematically, avoiding the requirement of accuracy measurement and complex system setup

in conventional methods. Different from the time-consuming process in obtaining the correct defocus distance, our method can obtain the defocus distance quickly on the algorithm. Furthermore, an accurate focusing process is not required in the proposed method. Finally, we use some biological samples and the AP phase retrieval method to demonstrate the feasibility of the proposed method in actual experiments, and a 3D localization corresponding to different defocus distances can be realized.

Although the effectiveness of our method has been proven, there are still some details that can be improved in further works. Firstly, the calculation accuracy of the defocus distance can be increased. In our paper, we use the SAD image registration method to calculate the pixel shift between channels, whose measurement accuracy will be half of a pixel. For further work, the measurement accuracy can be increased by the method proposed in [37]. Furthermore, the sub-pixel image registration method can also be implemented to increase the measurement accuracy. Secondly, theoretically, a larger illumination angle results in a more obvious separation between two channels. However, in actual experiments, considering the effective range of the bright field in oblique illuminations, the largest tangent

function between red and blue incident illumination is $\tan \theta_{rb} = \frac{5}{90}$, which results in unobvious separations between the two channels. In further works, we can use some binary lens designed by metamaterial to obtain a more obvious chromatic aberration in experiments.

DATA AVAILABILITY STATEMENT

The raw data supporting the conclusions of this article will be made available by the authors, without undue reservation.

AUTHOR CONTRIBUTIONS

SZ conceived the idea. GZ did the experiments and writing. SZ, YH, and QH supervised the project. All the authors contributed to the review.

FUNDING

This work was supported by the National Natural Science Foundation of China under grants 61875012, 51735002, 61735003, and 61805011.

REFERENCES

- Barty ANTON, Nugent KA, Paganin D, Roberts A. Quantitative optical phase microscopy. *Opt Lett.* (1998) 23:817–9. doi: 10.1364/OL.23.000817
- Choi W, Fang-Yen C, Badizadegan K, Oh S, Lue N, Dasari RR, et al. Tomographic phase microscopy. *Nat Methods.* (2007) 4:717–9. doi: 10.1038/nmeth1078
- Mann CJ, Yu L, Lo CM, Kim MK. High-resolution quantitative phase-contrast microscopy by digital holography. *Opt Express.* (2005) 13:8693–8. doi: 10.1364/OPEX.13.008693
- Marquet P, Rappaz B, Magistretti PJ, Cuche E, Emery Y, Colomb T, et al. Digital holographic microscopy: a noninvasive contrast imaging technique allowing quantitative visualization of living cells with subwavelength axial accuracy. *Opt Lett.* (2005) 30:468–70. doi: 10.1364/OL.30.000468
- Millerd J, Brock N, Hayes J, North-Morris M, Kimbrough B, Wyant J. *Pixelated Phasemask Dynamic Interferometers. Fringe 2005.* Berlin, Heidelberg: Springer (2006). p. 640–7.
- Paganin D, Nugent KA. Noninterferometric phase imaging with partially coherent light. *Phys Rev Lett.* (1998) 80:2586–9. doi: 10.1103/PhysRevLett.80.2586
- Tan Y, Wang W, Xu C, Zhang S. Laser confocal feedback tomography and nano-step height measurement. *Sci Rep.* (2013) 3:2971. doi: 10.1038/srep02971
- Zernike F. Phase contrast, a new method for the microscopic observation of transparent objects part II. *Physica.* (1942) 9:974–86. doi: 10.1016/S0031-8914(42)80079-8
- Allen RD, David GB, Nomarski G. The Zeiss-Nomarski differential interference equipment for transmitted-light microscopy. *Zeitschrift für wissenschaftliche Mikroskopie und mikroskopische Technik.* (1969) 69:193–221.
- Thibos LN. Principles of Hartmann-Shack aberrometry. *J. Refractive Surg.* (2000) 16:563–5. doi: 10.1364/VSIA.2000.NW6
- Platt BC, Shack R. History and principles of Shack-Hartmann wavefront sensing. *J Refract Surg.* (2001) 17:S573–7. doi: 10.3928/1081-597X-200109-13
- Zheng G, Horstmeyer R, Yang C. Wide-field, high-resolution Fourier ptychographic microscopy. *Nat Photonics.* (2013) 7:739–45. doi: 10.1038/nphoton.2013.187
- Zuo C, Sun J, Chen Q. Adaptive step-size strategy for noise-robust Fourier ptychographic microscopy. *Opt Express.* (2016) 24:20724–44. doi: 10.1364/OE.24.020724
- Bian L, Suo J, Zheng G, Guo K, Chen F, Dai Q. Fourier ptychographic reconstruction using Wirtinger flow optimization. *Opt Express.* (2015) 23:4856–66. doi: 10.1364/OE.23.004856
- Rodenburg JM, Faulkner HM. A phase retrieval algorithm for shifting illumination. *Appl Phys Lett.* (2004) 85:4795–7. doi: 10.1063/1.1823034
- Li G, Yang W, Wang H, Situ G. Image transmission through scattering media using ptychographic iterative engine. *Appl Sci.* (2019) 9:849. doi: 10.3390/app9050849
- Horstmeyer R, Chen RY, Ou X, Ames B, Tropp JA, Yang C. Solving ptychography with a convex relaxation. *New J Phys.* (2015) 17:053044. doi: 10.1088/1367-2630/17/5/053044
- Maiden AM, Humphry MJ, Zhang F, Rodenburg JM. Superresolution imaging via ptychography. *J Opt Soc Am A.* (2011) 28:604–12. doi: 10.1364/JOSAA.28.000604
- Gureyev TE, Roberts A, Nugent KA. Partially coherent fields, the transport-of-intensity equation, phase uniqueness. *J Opt Soc Am A.* (1995) 12:1942–6. doi: 10.1364/JOSAA.12.001942
- Gureyev TE, Roberts A, Nugent KA. Phase retrieval with the transport-of-intensity equation: matrix solution with use of Zernike polynomials. *J Opt Soc Am A.* (1995) 12:1932–41. doi: 10.1364/JOSAA.12.001932
- Zuo C, Chen Q, Asundi A. Boundary-artifact-free phase retrieval with the transport of intensity equation: fast solution with use of discrete cosine transform. *Opt Express.* (2014) 22:9220–44. doi: 10.1364/OE.22.009220
- Zhang J, Chen Q, Sun J, Tian L, Zuo C. On a universal solution to the transport-of-intensity equation. *Opt Lett.* (2020) 45:3649–52. doi: 10.1364/OL.391823
- Wittkopp JM, Khoo TC, Carney S, Pisila K, Bahreini SJ, Tubbesing K, et al. Comparative phase imaging of live cells by digital holographic microscopy and transport of intensity equation methods. *Opt Express.* (2020) 28:6123–33. doi: 10.1364/OE.385854
- Marchesini S. Invited article: a unified evaluation of iterative projection algorithms for phase retrieval. *Rev Entific Instr.* (2007) 78:229–61. doi: 10.1063/1.2403783
- Waller L, Kou SS, Sheppard CJ, Barbastathis G. Phase from chromatic aberrations. *Opt Express.* (2010) 18:22817–25. doi: 10.1364/OE.18.022817

26. Komuro K, Nomura T. Quantitative phase imaging using transport of intensity equation with multiple bandpass filters. *Appl Opt.* (2016) 55:5180–6. doi: 10.1364/AO.55.005180
27. Kakei S, Komuro K, Nomura T. Transport-of-intensity phase imaging with polarization directed flat lenses. *Appl Opt.* (2020) 59:2011–5. doi: 10.1364/AO.386020
28. Komuro K, Saita Y, Tamada Y, Nomura T. Numerical evaluation of transport-of-intensity phase imaging with oblique illumination for refractive index tomography. In: *Digital Holography and Three-Dimensional Imaging 2019, OSA Technical Digest (Optical Society of America, 2019), paper Th3A.37.*
29. Guo C, Bian Z, Jiang S, Murphy M, Zhu J, Wang R, et al. OpenWSI: a low-cost, high-throughput whole slide imaging system via single-frame autofocusing and open-source hardware. *Opt Lett.* (2020) 45:260–3. doi: 10.1364/OL.45.000260
30. Guevorkian D, Launiainen A, Liuha P, Lappalainen V. Architectures for the sum of absolute differences operation. In: *Signal Processing Systems. IEEE.* (2002). p. 57–62.
31. Silveira B, Paim G, Abreu B, Grellert M, Diniz CM, da Costa EA, et al. Power-efficient sum of absolute differences architecture using adder compressors. In: *2016 IEEE International Conference on Electronics, Circuits and Systems (ICECS).* IEEE (2016).
32. Lee W, Jung D, Ryu S, Joo C. Single-exposure quantitative phase imaging in color-coded LED microscopy. *Opt Express.* (2017) 25:8398. doi: 10.1364/OE.25.008398
33. Phillips ZF, Chen M, Waller L. Single-shot quantitative phase microscopy with color-multiplexed differential phase contrast (cDPC). *PLoS ONE.* (2017) 12:e0171228. doi: 10.1371/journal.pone.0171228
34. Netrapalli P, Jain P, Sanghavi S. Phase retrieval using alternating minimization. *IEEE Trans Signal Process.* (2015) 63:4814–26. doi: 10.1109/TSP.2015.2448516
35. Fienup JR. Phase retrieval algorithms: a comparison. *Appl Opt.* (1982) 21:2758–69. doi: 10.1364/AO.21.002758
36. Voelz DG. *Computational Fourier Optics: A MATLAB Tutorial.* Las Cruces, NM: SPIE (2011).
37. Zhou G, Zhang S, Hu Y, Hao Q. Single-shot sequential projection phase retrieval and 3D localization from chromatic aberration. *Opt Express.* (2020) 28:9976–87. doi: 10.1364/OE.389260

Conflict of Interest: The authors declare that the research was conducted in the absence of any commercial or financial relationships that could be construed as a potential conflict of interest.

Copyright © 2021 Zhou, Zhang, Zhai, Hu and Hao. This is an open-access article distributed under the terms of the Creative Commons Attribution License (CC BY). The use, distribution or reproduction in other forums is permitted, provided the original author(s) and the copyright owner(s) are credited and that the original publication in this journal is cited, in accordance with accepted academic practice. No use, distribution or reproduction is permitted which does not comply with these terms.